



Simultaneous slit rheometry and in situ neutron scattering

Javen S. Weston^{1,2} · Daniel P. Seeman³ · Daniel L. Blair¹ · Paul F. Salipante² · Steven D. Hudson² · Katie M. Weigandt³

Received: 22 September 2017 / Revised: 11 January 2018 / Accepted: 14 January 2018 / Published online: 12 February 2018
© Springer-Verlag GmbH Germany, part of Springer Nature 2018

Abstract

In situ measurement of fluid structure during flow, e.g., by neutron scattering, is key to understanding the relationship between structure and rheology. For some applications, structures at high shear rates previously unreachable are of particular interest. Here, we report development of a flow cell slit rheometer for neutron scattering (μ RheoSANS). The devices were used to measure the structure of a semi-dilute surfactant solution of worm-like micelles during flow. Analysis of the rheometry and scattering data allows isolation of the scattering signal from the high-shear, near-wall region of the flow cell. The reported results agree with those from the existing Couette-based RheoSANS instrument. The worm-like micelles exhibit an alignment transition at Weissenberg number (Wi) ≈ 1 , coinciding with the onset of shear thinning. This transition is followed by a peak in micelle alignment at a higher shear rate, after which the degree of alignment decreases moderately. This technique can achieve higher shear rates than existing RheoSANS techniques, expanding the ability to study the structure of complex fluids at elevated shear rates.

Keywords Worm-like micelles · Slit flow · Scattering

Introduction

Complex fluids undergo deformation at extreme shear rates in a variety of commercial processes such as spraying, coating, syringe injection, filtration, oil extraction, lubrication, and extrusion. Therefore, accurately measuring the flow properties of fluids at deformation rates up to approximately 10^6 s^{-1} is highly relevant and an important area of research. Two different methods to generate high shear rates have proven

successful: (1) parallel plate geometries using very small gaps ($\sim 30 \text{ }\mu\text{m}$) and (2) pressure-driven flow through small slits or capillaries (Pipe et al. 2008). Advances in the manufacture and design of microfluidic devices have resulted in the latter option becoming a popular way to measure fluid properties at high shear rates (Hudson et al. 2015; Moon and Migler 2009; Pipe and McKinley 2009; Squires and Quake 2005). The small characteristic length scales used in microfluidic devices ($< 100 \text{ }\mu\text{m}$) also provide other advantages in comparison to traditional macroscopic rheometric devices. For instance, measurements can be made using smaller sample volumes, and certain types of flow instabilities are more easily avoided. Specifically, microfluidic channels allow for higher shear rates to be reached while maintaining sufficiently low Reynolds numbers to avoid inertially driven flow instabilities. Small angle neutron scattering, when paired with flow and rheometric measurements, has proven to be a useful tool for determining how shear affects the microstructure of a wide variety of soft matter systems (Eberle and Porcar 2012), including proteins (Singh et al. 2009; Weigandt et al. 2011), liquid crystals (Noirez and Lapp 1997), emulsions (Mason et al. 2006), nanoparticle dispersions (Krishnamurthy et al. 2003; Maranzano and Wagner 2002), and numerous micellar systems (Gaudino et al. 2017; Liberatore et al. 2006; Lopez et al. 2015; Penfold et al. 2006; Takeda et al. 2011), among others.

Electronic supplementary material The online version of this article (<https://doi.org/10.1007/s00397-018-1073-0>) contains supplementary material, which is available to authorized users.

✉ Steven D. Hudson
steven.hudson@nist.gov

✉ Katie M. Weigandt
kathleen.weigandt@nist.gov

¹ Department of Physics and Institute for Soft Matter Synthesis and Metrology, Georgetown University, Washington, DC, USA

² Materials Science and Engineering Division, National Institute of Standards and Technology, Gaithersburg, MD, USA

³ Center for Neutron Research, National Institute of Standards and Technology, Gaithersburg, MD, USA

Worm-like and rod-like micelle solutions are a model system for studying flow phenomena of non-Newtonian, viscoelastic fluids (Bernheim-Groswasser et al. 2000; Berret et al. 2001; Koehler et al. 2000; Lindner et al. 1990; Lutz-Bueno et al. 2013; Magid et al. 2000; Takeda et al. 2011; Walker 2001). Neutron scattering is particularly well suited to study micellar systems due to the ability to resolve relevant length scales and to vary or enhance contrast through use of isotopic substitution. The contrast between D₂O and the hydrocarbon tail groups of the surfactant molecules generates a strong scattering signal that allows data collection times to be relatively short at each set of conditions. The particular surfactant system studied here is a commonly used model (Amin et al. 2015; Vogtt et al. 2015; Zou et al. 2015) and is relevant in a variety of commercial applications including detergents and shampoos. We use a semi-dilute solution with a monotonic stress vs shear rate dependence in an attempt to avoid flow instabilities related to shear banding (Fardin et al. 2016; Fardin et al. 2014; Morozov and van Saarloos 2007) that would complicate data analysis.

Here, we describe the development of a device using a slit capillary to carry out simultaneous rheological and microstructural characterization of complex fluids (referred to as μ RheoSANS) and compare the experimental results of Couette and Poiseuille RheoSANS. The Couette geometries currently used for RheoSANS techniques are limited to shear rates of $< 10,000 \text{ s}^{-1}$, while capillary and slit rheometers like the one described here can achieve wall shear rates 1–2 orders of magnitude higher. We use a rectangular slit with a slit height approximately 100 μm to make viscometric measurements at relatively high shear rates, while simultaneously illuminating the flow path with a neutron beam to measure the sample scattering and characterize how the microstructure of the fluid sample changes during shear deformation. We evaluate the degree of alignment achieved over a range of shear rate, as accessible in each geometry.

Materials and methods

The fluids used in this study are simple aqueous solutions containing a sodium lauryl ether sulfate (SLE-3-S) surfactant and various concentrations of sodium chloride to control the micelle morphology. The sodium lauryl ether sulfate (nominally $\text{NaSO}_4(\text{CH}_2\text{CH}_2\text{O})_3 \text{C}_{12}\text{H}_{25}$) under the trade name of Steol CS-460 was obtained from the Stepan Company as an aqueous solution with an active mass fraction of 60% and the remainder being water (approx. 25% mass fraction), ethanol (approx. 15% mass fraction), and a small amount of unsulfated fatty alcohols (approx. 2.5% mass fraction). The surfactant was used as received without any additional purification steps. This surfactant is typically used for personal care products and contains surfactant molecules with a distribution

of number of ethoxylate groups per molecule. Therefore, all tested samples will list surfactant concentrations on a mass fraction of active surfactant basis rather than mol/L, etc. Reagent grade ($> 99.0\%$) sodium chloride was purchased from Fisher Scientific and used as received. All D₂O was obtained from Cambridge Isotope Laboratories, Inc. at 99.9% purity and used as received. Micellar solutions were prepared by dissolving the required amount of NaCl in pure D₂O at room temperature and then subsequently adding the surfactant solution to reach a final mass fraction of 1.15% SLE-3-S active surfactant and (5 to 11) % mass fraction NaCl.

Type 48 linear flow cells designed for use in spectrophotometers were purchased from Starna Cells, Inc. The cell flow paths are 33 mm long, 8 mm wide, and available in a variety of heights; this study was completed using cells with nominal channel heights of 100 μm (Fig. S2 contains a schematic of the flow cell geometry). The cells come with barb-style hose connections, which were removed using a diamond saw to create a flat sealing surface. A pair of custom flow adapters was designed and use fluoropolymer O-rings to seal onto the inlet and outlet of the flow cell. The remaining plumbing is completed using standard compression fittings and 1/8" OD–1/16" ID HDPE tubing. A pair of NE-1010 FW-1-X2 syringe pumps was used to push the fluid through the flow cell at a constant flow rate.

Pressure drops across the cell channel were monitored using MPS microfluidic pressure sensors purchased from Elveflow. A combination of 1 bar and 7 bar sensors was used to maximize measurement sensitivity, which is 0.1% of full scale for both sensors. The pressure sensors were placed as close as possible to the inlet and outlet of the flow channel to minimize the influence of the tubing pressure drop (approx. 50 mm of 1/16" ID tubing separated the pressure sensors from the inlet/outlet of the flow channel). Pressure drops across the flow adapters and tubing were measured at all tested flow rates using a specially designed bypass flow channel (33 mm long, 8 mm wide, 2-mm height) that provides a negligible contribution to the pressure drop. These pressure drops were then subtracted from the pressure drops measured during experiments to isolate the pressure drop across the flow channel alone. Additional experiments were conducted using two Newtonian fluids (deionized water and propylene glycol) to determine the viscometric resistance of each flow channel and compare it to the expected resistance for a channel with the nominal channel dimensions. Details and data from these experiments are available in the [Supplementary Information](#).

RheoSANS and μ RheoSANS experiments were carried out at the NIST Center for Neutron Research using the NG7, NGB 30 m, and NGB 10 m SANS instruments. RheoSANS experiments were carried out using the standard Anton-Paar MCR 501 rheometer with a Couette geometry specially designed for RheoSANS consisting of a titanium bob (28-mm diameter) and cup (30-mm diameter). Data was collected and

reduced to absolute scale using standard NCNR protocols in the Igor Pro software package (Kline 2006). Micelle alignment was calculated using annular averages of the 2D scattering patterns at $0.02 \text{ \AA}^{-1} < q < 0.03 \text{ \AA}^{-1}$. The annular averages were fit to an even Legendre polynomial expansion model where the second coefficient provides an alignment factor (P2). All rheometric data not collected using the μ RheoSANS device was measured using an Anton-Paar MCR 501 rheometer with various Couette geometries.

Results

Motivation and sample characterization

The central goal of this work is to demonstrate that a slit capillary scattering cell can be used to accurately characterize the rheological properties and fluid microstructure in a way that can be compared to the large body of literature involving simultaneous small angle scattering and rheological characterization. To establish this connection, the rheology and static neutron scattering must first be explored to determine the micelle properties. The worm-like micelle region was first mapped out by varying the salt concentration at a fixed surfactant concentration (inset of Fig. 1a). Over a broad range of compositions, worm-like cylindrical micelles are formed. Changing salt concentration adjusts the effective shape of the surfactant molecule by modifying the relative energy required to form the high-curvature endcaps of the cylindrical micelle. The energy penalty for creating an endcap controls the equilibrium micelle length and produces dramatic changes in the solution viscosity (Porte et al. 1986). The dramatic increase in viscosity at intermediate salt mass fractions arises from entanglement of the micelles. At a critical salt concentration (above 11% mass fraction; see Fig. 1a, inset), the viscosity decreases again when the micelles become branched (Calabrese et al. 2015; Gaudino et al. 2015). Further increasing salt concentration results in more prevalent branching and even lower viscosity. Eventually, precipitation or phase separation occurs. At a mass fraction of 1.15%, the surfactant used here becomes entangled at a salt mass fraction of $\approx 6\%$ and the zero shear viscosity peaks at $\approx 11\%$ mass fraction, above which the viscosity sharply decreases and precipitation is observed at salt mass fractions $\geq 13\%$. We chose to use a sample with a 1.15% surfactant mass fraction ($C_{M,\text{surf}}$) and 8.0% salt mass fraction ($C_{M,\text{sal}}$) as our model system during initial testing of the μ RheoSANS device. This formulation is well below the critical salt mass fraction where branching occurs. The sample viscosity is sufficiently low such that the shear thinning transition can be observed well beyond shear rates measured with traditional RheoSANS without exceeding the torque limit of our syringe pump. Finally, the sample is weakly entangled, implying that the micelles will undergo

appreciable alignment under shear, but without the presence of a stress plateau that can result in shear banding for more entangled micelle solutions (note: a stress plateau would appear as a power law slope of -1 on a plot of viscosity vs shear rate; the power law slope of this sample is only -0.67). Furthermore, the straight flow channel should aid in suppressing the onset of elastic flow instabilities caused by curved streamlines (Pakdel and McKinley 1996). However, pressure-driven flow of non-Newtonian fluids in microfluidic channels has been shown to cause a variety of spatiotemporal flow instabilities that must be avoided or taken into account during experimentation (Bécu et al. 2004; Haward et al. 2014; Méndez-Sánchez et al. 2003; Salipante et al. 2017).

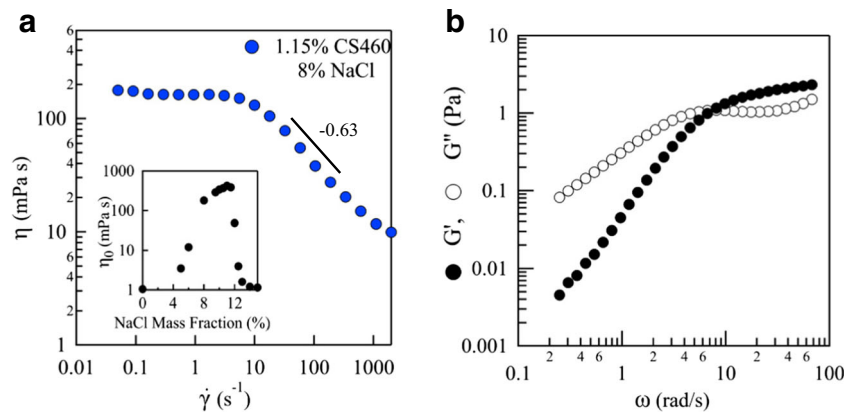
As such, the sample exhibits rheology typical of weakly entangled worm-like living chains (Fig. 1). Specifically, in steady flow, the fluid is Newtonian at low shear rates and shear thinning at higher rates (Fig. 1a), and the linear viscoelastic moduli (Fig. 1b) show the corresponding crossover from viscous to elastic behavior. The longest relaxation time indicated by the low-frequency crossover of moduli (at $\omega \approx 7 \text{ rad/s}$) corresponds to the onset of shear thinning in steady shear flow. The rheological properties and associated longest relaxation times of entangled micellar solutions are largely controlled by micelle diffusion (reptation) and continual equilibration of the micelle size (breakage and reformation) (Cates and Candau 1990; Rehage and Hoffmann 1991). Faster relaxation processes (such as a so-called breathing mode) are also active, and these details manifest in features such as the frequency of a local minimum of G'' at high frequency and in the shear thinning slope of the flow curve. For our proposed model system, oscillatory rheology provides us with values for the plateau modulus (G_N) and high-frequency minimum of the loss modulus (G''_{min}) of 2.31 and 0.94 Pa, respectively. These rheological features provide a measure of various structural and dynamic properties of the worm-like micelles. Applying Granek and Cates's (1992) formula for the micelle length:

$$(L/l_e) = (G_N/G''_{\text{min}})^{1.25} \quad (1)$$

where L is the number average micelle length and l_e is the length between entanglements; the micelles in the sample are thus moderately entangled, with L being greater than l_e . In the present case, this formula is a rough approximation since the frequencies associated with the crossover and G''_{min} are not widely separated. Higher frequency rheological data, which could be obtained via diffusing wave spectroscopy, along with use of Zou and Larson's (2014) "pointer" simulation method could be used for more accurate analysis.

To determine the persistence length of the micelles, quiescent neutron scattering covering a q range of $0.0014\text{--}0.7 \text{ \AA}^{-1}$ was used. Small angle scattering from dilute worm-like chains is well understood (Higgins et al. 1994): at high q , scattering intensity decays as q^{-4} ; a transition to q^{-1} dependence occurs

Fig. 1 **a** Steady shear rheology at 22.5 °C for the studied system along with (inset) the evolution of zero shear viscosity as a function of NaCl mass fraction. **b** Oscillatory frequency sweep of model micelle solution at 22.5 °C at a strain amplitude of 1%



at a q value corresponding to the diameter of the micelle. Then, in ideal worm-like chains scattering, intensity transitions to q^{-2} dependence below a q corresponding to the persistence length of the chain segments. Finally, below a q corresponding to the coil size of the chain, scattering intensity becomes independent of q . However, the overlap and entanglement of these worm-like micelles significantly affects their scattering. To test whether the scattered intensity at lowest q is limited by the micelle size or by the structure factor (intermicellar interference), a range of surfactant concentrations were tested using SANS (shown in [Supplemental Information](#)). Decreasing the surfactant concentration should decrease micelle size, with $L \propto c^{0.5}$ and below a critical surfactant concentration (C_{surf}^*), the micelles do not experience excluded volume effects, and the scattering structure factor is equal to unity at all q (Pedersen and Schurtenberger 1996). Persistence length (l_p) is then determined by fitting the scattering at a concentration $< C_{\text{surf}}^*$ to a flexible chain scattering model (Pedersen 1997) while factoring in polydispersity in the micelle contour length using a Flory-Schulz distribution. Failing to include a logical polydispersity in contour length would result in an overestimation of the persistence length due to the suppression in low q scattering resulting from the presence of population of short micelles. Additional experiments carried out at lower surfactant concentrations also indicate that the persistence length does not vary with surfactant concentration. For the model fluid, l_p was found to be ≈ 28 nm.

Device evaluation

Particle image velocimetry (PIV) measurements were conducted to measure the velocity profile across the width (8-mm dimension) of the cell (Fig. 2), for wall shear rates ranging from 120 to 3200 s^{-1} . As required for accurate rheometry and scattering analysis, the flow is indeed uniform across the width, approximating planar flow between two flat plates in the region probed by SANS. Information and a detailed discussion of flow conditions that can result in non-negligible width-wise velocity gradients can be found in Salipante

et al. (2017). No measurable spatial or temporal instability is observed in the flow cell.

In plane Poiseuille flow of non-Newtonian fluids, the velocity profile (now in the gap or height direction) deviates from the ideal parabola. Accordingly, true wall shear rates in the slit rheometer were obtained through the Rabinowitsch correction. Steady shear rheology measured using the Couette RheoSANS and Poiseuille μ RheoSANS devices show excellent overlap across the approx. 2 orders of magnitude in shear rate accessible to both rheometers (Fig. 3). The device can effectively measure steady shear viscosities that are directly comparable to simple shear data collected at lower shear rates.

Simultaneous SANS measurements conducted using the device can be used to easily track changes in complex fluid microstructure. Here, we track bulk micelle alignment as a function of shear rate by quantifying the degree of scattering anisotropy at a fixed q . However, the device could also be used to track shear-induced colloidal cluster breakup (Wilking et al. 2011), deformation (Chatterjee et al. 2014), or other microstructural changes at SANS length scales. An alignment factor was determined from a model fit of annular measurements of the 2D scattering patterns (Burger et al. 2010). A transition from isotropic to anisotropic scattering was observed in both rheometers (Fig. 3, bottom). The transition occurs at $\dot{\gamma} \approx 20 \text{ s}^{-1}$ in the Couette geometry (red Xs in Fig. 3, bottom) and $\dot{\gamma} \approx 100 \text{ s}^{-1}$ in the Poiseuille geometry (blue filled circles in Fig. 3, bottom). The alignment observed in the slit rheometer is also lower than that of the Couette cell. Alignment increases sharply above the critical shear rate and reaches a peak alignment at approx. 600 s^{-1} . Above this shear rate, alignment then decreases to a plateau value. The μ RheoSANS alignment behaves as expected relative to the RheoSANS because the microfluidic channel contains both well-aligned micelles near the channel wall along with more isotropic micelles near the channel center. In Couette flow, there is an essentially linear velocity gradient in the gap between the two cylinders, resulting in the entire sample being deformed at a nearly uniform shear rate (unless wall slip, shear

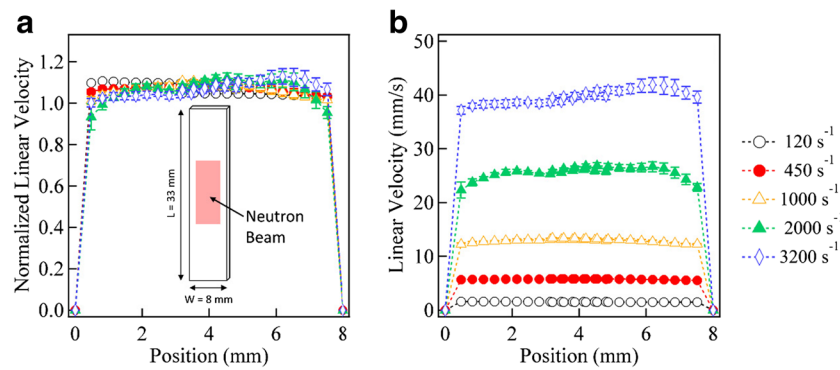


Fig. 2 Width-wise velocity profiles on a normalized (a) and absolute (b) velocity scale measured using particle imaging velocimetry at a variety of wall shear rates. Note that the velocity profile here is not the velocity profile across the height of the channel. Experiments show that fluid velocity is

essentially constant across the channel width, justifying the assumption of approximately planar flow between two flat plates. Error bars on data points represent standard deviations calculated using a 95% confidence interval

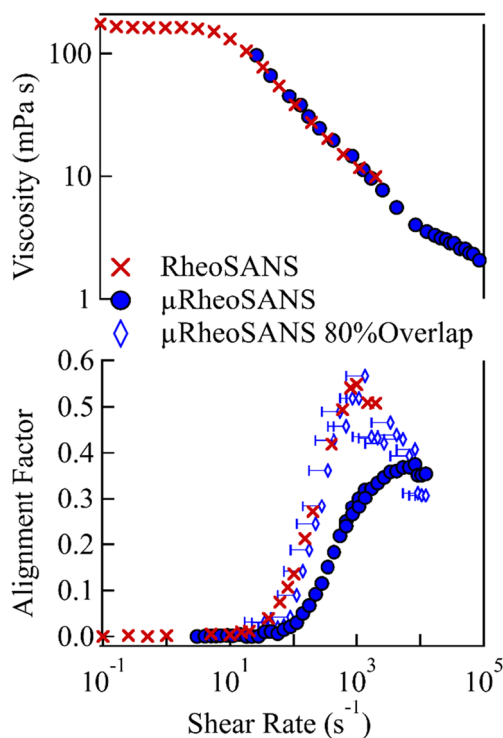


Fig. 3 Rheology and micelle alignment data from RheoSANS and μRheoSANS experiments using a SLE-3-S micelle solution at 8% NaCl. Reported μRheoSANS shear rates are wall shear rates and have been corrected for non-parabolic velocity profiles. Flow curve data (top) from the two techniques overlap for more than one order of magnitude and strongly agree. After subtraction-based analysis technique, micelle alignment plots for the two techniques also show good agreement; the peak in alignment factor is even recovered following subtraction. For the post-subtraction data, diamond symbols represent the wall shear rate, while the horizontal bar indicates the range of shear rates present in the isolated, near-wall scattering region. The μRheoSANS flow curve extends farther than the corresponding alignment factor data because of volume limitations of the syringes used in the experiments. The syringes contain enough volume to measure a steady state viscosity at very high flow rates, but larger syringes would be necessary to easily carry out a neutron scattering experiment at those flow rates. The rheology data is shown to demonstrate that the device is capable of reaching shear rates of O (100,000 s⁻¹), but SANS measurements are not yet feasible at those shear rates

banding, or other flow instabilities occur). The Poiseuille flow in the μRheoSANS cell results in a distribution of shear rates across the height of the channel with a maximum shear rate at the channel walls and a shear rate of zero at the channel center. SANS patterns collected with the neutron beam passing through the full height of the channel (as done here) will be convolutions of all the shear rates present in the channel. Therefore, it is not useful to directly compare raw alignment factors collected in these experiments to Couette RheoSANS data for the same sample. However, Poiseuille flow is prevalent in a wide variety of industrial and biological processes, and the μRheoSANS device could be used to characterize flow profiles relevant to these applications. The flow cell produces very little background scattering over the full range of q , and μRheoSANS measurement times are comparable to RheoSANS experiments conducted in the flow and vorticity planes. As with other neutron-based techniques, contrast-matching could also be used to isolate scattering resulting from specific constituents of multi-component systems. All of which combine to result in a powerful tool for characterizing complex fluids undergoing Poiseuille flow.

The ability to isolate scattering from the high-shear, near-wall region of the slit capillary would allow for a direct comparison of Couette and Poiseuille RheoSANS and greatly extend the range of shear rates that can be probed using neutron scattering. As mentioned previously, continuous fluids undergoing pressure-driven flow experience a maximum stress at the wall (τ_{wall}). From the wall, the stress decreases linearly to zero at the center of the channel, as shown in Fig. 4. This behavior holds for Newtonian, shear thinning, and shear banding fluids and allows the velocity and shear rate profiles for a fluid to be calculated if the steady shear rheology is known and well behaved.

Using this relationship, a data analysis technique analogous to those of Tang et al. (1984) and Fernandez-Ballester et al. (2009) can be used to isolate the scattering resulting from the high-shear, near-wall region of the flow cell by collecting

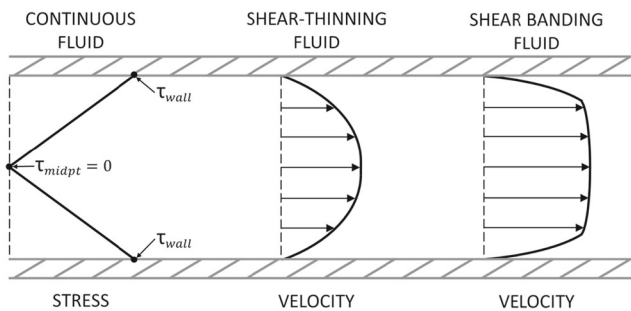


Fig. 4 Schematic of Poiseuille flow across the height of a microchannel. Example velocity profiles shown for two cases: shear thinning and shear banding fluids assumes a linear relationship between shear stress, τ , and channel height, such that stress goes to zero at the midpoint of the channel. This linear stress relationship is valid for both cases

scattering patterns at two different flow rates (Q_n and Q_{n-1}), where the wall stresses are $\tau_{w,n}$ and $\tau_{w,n-1}$. Since stress always varies linearly from a maximum at the wall to zero in the center of the channel and $\tau_{w,n} > \tau_{w,n-1}$, the stress $\tau_{w,n-1}$ occurs at some point in the stress profile of the higher flow experiment. From that point towards the channel center, the fluid's shear rate profile will be the same as that of the full channel in the Q_{n-1} experiment, but confined to a fraction of the channel height proportional to the ratio of the wall stresses,

$$\tau_{ratio} = \frac{|\tau_{w,n-1}|}{|\tau_{w,n}|} \quad (2)$$

The difference in the two scattering patterns is coming from the near-wall region only. Using this relationship, the high-shear, near-wall scattering pattern can be isolated using the equation below:

$$I(q_x, q_y)_{near-wall} = \frac{1}{1 - \tau_{ratio}} \left[I(q_x, q_y)_n - \tau_{ratio} \left(I(q_x, q_y)_{n-1} \right) \right] \quad (3)$$

where $I(q_x, q_y)_z$ is the scattering intensity at the point (q_x, q_y) for flow rate z . Additionally, more detailed discussion of this subtraction analysis, with corresponding figures, can be found in the [Supplemental Information](#). We note the following caveat. The results of this analysis technique would be inaccurate if the sample scattering is a function of more than just shear stress. For instance, flow-induced concentration gradients or inertial migration of particle suspensions would not be accounted for in this procedure. The technique also depends on the assumption that sample scattering is not strongly affected by changes in the stress gradient across the channel, i.e., that the rheology is determined locally, by the local stress alone. These abnormalities could be minimized by using small variations in flow rate/wall stress, so that τ_{ratio} is close to unity. However, as τ_{ratio} approaches 1, the signal-to-noise ratio in the resultant scattering pattern will be greatly decreased, requiring longer scattering experiments and better measurement

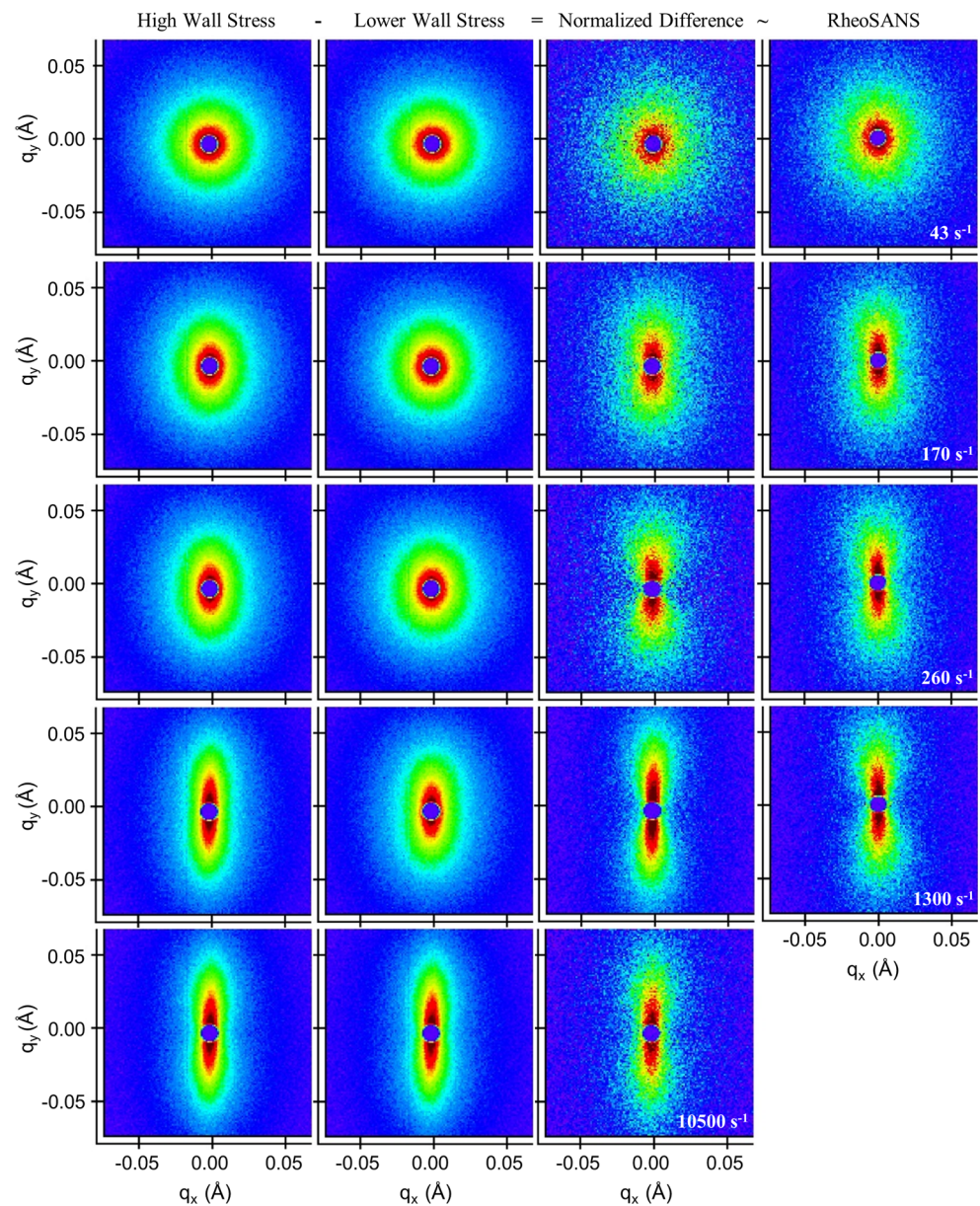
statistics to compensate (see Fig. [S6](#) and associated discussion in [Supplemental Information](#)). A collection of scattering patterns for the high flow rate, low flow rate, resultant near-wall scattering, and Couette RheoSANS scattering at an equivalent shear rate are shown in Fig. [5](#).

Conducting this data analysis technique on the SANS patterns obtained from our model system results in a distinct shift in the alignment vs shear behavior (blue diamonds in Fig. [3](#), bottom) when compared to that of the full channel (blue circles, same plot). In the figure, the blue diamond symbols represent the wall shear rate in the microfluidic channel, while the horizontal bar indicates the range of shear rates present in the isolated, near-wall scattering region. The experiments here were conducted using a planned set of flow rates that would result in a stress ratio ≈ 0.8 for all subtractions. Therefore, the resulting scattering patterns correspond to the structure from the sample located within $10 \mu\text{m}$ of the channel walls. This amount of overlap provides a good balance between experimental beam time limitations and the ability to isolate high-shear scattering. The optimum overlap ratio will depend on the geometry of the channel, how strongly the sample scatters, and the q range being probed.

After isolating the high-shear scattering, the alignment vs shear behavior in the $\mu\text{RheoSANS}$ data shows excellent agreement with the RheoSANS data. Micelle alignment occurs at essentially the same critical shear rate, the growth of alignment is similar, and the peak in alignment is even recovered. Overall, the experiments demonstrate that the subtraction data analysis technique is effective at isolating the near wall scattering and can be used to recover structural information similar to that obtained in standard RheoSANS experiments.

Although they provide a powerful visual aid, the 2D scattering patterns shown in Fig. [5](#) are difficult to directly compare, despite being reduced to absolute scale and plotted on identical color maps. Therefore, additional, 1D scattering plots are shown in Fig. [6](#) to further illustrate the ability of this analysis to provide scattering data that can be compared directly to that collected using traditional Couette RheoSANS geometries. It is important to note, again, that all the scattering data shown in Figs. [5](#) and [6](#) are plotted on absolute scale, with no scaling factors used to adjust the data post-reduction. Comparing circular averages of Couette RheoSANS data under static and shearing conditions (Fig. [6a](#)) demonstrates a commonly observed reduction in overall scattering intensity in complex fluids that align under shear. This occurs because anisotropic objects scatter more strongly in the direction transverse to their length and under shear fewer micelle segments are oriented in the velocity-gradient directions, reducing the amount of transverse scattering in the radial beam path and shifting that scattering intensity out of plane, and thus undetected. Sector averages taken in the direction of alignment (Fig. [6a](#)) show that the scattering at zero shear is

Fig. 5 Array of 2D scattering patterns obtained at $0.009 \text{ \AA}^{-1} < q < 0.084 \text{ \AA}^{-1}$ from μ RheoSANS and RheoSANS experiments illustrating the results of the subtraction data analysis. All scattering patterns are reduced to absolute scale and plotted using the same color map. From left to right, columns contain scattering patterns of (1) raw scattering at a given flow rate, (2) raw scattering at a slightly lower flow rate where the wall stress is approx. 80% of the wall stress of the flow rate from column 1, (3) scattering pattern obtained from using proposed subtraction technique, (4) scattering patterns measured using Couette RheoSANS at shear rates comparable to the wall shear rates isolated by the subtraction technique. Rows are ordered by nominal shear rate with shear rate increasing from top to bottom



isotropic (no difference between circular and sector averages for 0 s^{-1}) and that orientation strongly increases the scattering perpendicular to the flow direction. This increase in scattering perpendicular to flow (along with a simultaneous and larger decrease in scattering parallel to the flow direction) can also be seen when comparing annular averages of the same data (Fig. 6b). Sector (Fig. 6c) and annular (Fig. 6d) averages of a set of scattering patterns in Fig. 5 (middle row) where $\dot{\gamma} = \dot{\gamma}_{\text{wall}} = 260 \text{ s}^{-1}$ illustrate the ability of the subtraction technique to isolate the scattering from the near-wall, high-stress region of the microfluidic channel with good quantitative agreement between Couette and Poiseuille flow geometries being achieved when comparing all results on absolute scale.

The appearance of an alignment peak in both Couette and Poiseuille flow geometries suggest that this feature is a shear or stress-induced phenomenon and not simply the result of a flow instability, and the resulting secondary flows. In most literature studies, micelle alignment becomes saturated and reaches a plateau value at elevated shear rates. There is at least one case where a loss of alignment at highest rates has been observed in worm-like micelles (Castelletto and Hamley 2006; Castelletto et al. 2007). In that case, the scattering became completely isotropic after going through a range of shear rates where alignment was observed. Interrogating the cause of this alignment peak, along with its dependence on sample composition and experimental conditions, is the subject of ongoing research.

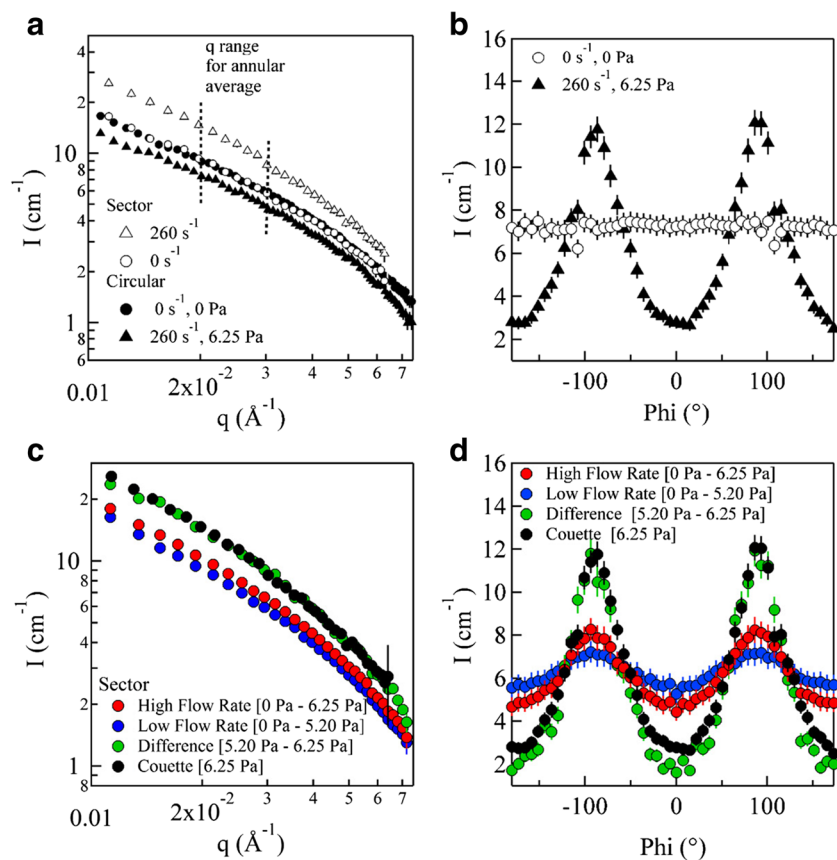


Fig. 6 Circular, sector, and annular average plots on absolute scale for selected Couette RheoSANS and μ RheoSANS data. **a** Circular averages of the WLM solution at rest and under Couette shear illustrate a decrease in scattering intensity commonly observed in systems that align under shear. **b** Annular averages of the scattering intensity for $0.02 \text{ \AA}^{-1} < q < 0.03 \text{ \AA}^{-1}$ (q range between two dashed lines in **a**) further illustrate the decrease in overall scattering as the regions of depressed scattering are much larger than the regions of increased scattering. **c** Sector averages (sampling a sector 15° wide in the direction of alignment) of the scattering

Discussion

A slit rheometer was used in conjunction with SANS measurements to characterize the structure and rheology of a non-Newtonian micellar solution. A data analysis technique was used to isolate the scattering resultant from the high-shear region of the flow channel, and these results were compared to measurements taken of the same fluid using a Couette RheoSANS device. Following corrections for non-parabolic velocity profiles and isolation of the near-wall scattering pattern, strong agreement is found between the two techniques. The micelles reached maximum alignment near a shear rate of 1000 s^{-1} . This slit-flow μ RheoSANS method is promising for future investigation of other interesting non-Newtonian fluids, such as shear banding and shear-thickening fluids. Current work is also underway to greatly expand the capabilities of the current device to

patterns in Fig. 5 (middle row) where $\dot{\gamma} = \dot{\gamma}_{\text{wall}} = 260 \text{ s}^{-1}$ illustrate the ability of the subtraction technique to reasonably isolate the scattering from the near-wall, high-stress region of the microfluidic channel. **d** Annular averages of these same scattering patterns further demonstrate that, after using the analysis technique described in the text to remove scattering contributions from the low-stress region of the channel, quantitative agreement between Couette and Poiseuille flow geometries can be achieved

increase (1) the maximum pressure the channel can contain from ≈ 3.5 bar to 350 bar, (2) the maximum shear rate the channel can probe from $\approx 1.5 \times 10^5 \text{ s}^{-1}$ to approx. $1.5 \times 10^6 \text{ s}^{-1}$ (depends on infinite shear viscosity of fluid), and (3) the ability to control sample temperature in a range from 0 to $150 \text{ }^\circ\text{C}$.

Acknowledgments This work benefited from the use of the SasView application, originally developed under NSF Award DMR-0520547. SasView also contains code developed with funding from the EU Horizon 2020 program under the SINE2020 project grant no. 654000. Commercial products mentioned in this work are listed for the purpose of fully describing the experiment and are not an endorsement by the National Institute of Standards and Technology. Access to *NGB30m SANS* was provided by the Center for High Resolution Neutron Scattering, a partnership between the National Institute of Standards and Technology and the National Science Foundation under Agreement No. DMR-1508249. JSW and DLB acknowledge support from Cooperative Agreement No. 70NANB15H229 from NIST, US Department of Commerce.

Compliance with ethical standards

Conflict of interest The authors declare that they have no conflict of interest.

References

- Amin S, Blake S, Kennel R, Lewis E (2015) Revealing new structural insights from surfactant micelles through DLS, microrheology and Raman spectroscopy. *Materials* 8(6):3754–3766. <https://doi.org/10.3390/ma8063754>
- Bécu L, Manneville S, Colin A (2004) Spatiotemporal dynamics of wormlike micelles under shear. *Phys Rev Lett* 93(1):018301. <https://doi.org/10.1103/PhysRevLett.93.018301>
- Bernheim-Groswasser A, Wachtel E, Talmon Y (2000) Micellar growth, network formation, and criticality in aqueous solutions of the non-ionic surfactant C12E5. *Langmuir* 16(9):4131–4140. <https://doi.org/10.1021/la991231q>
- Berret JF, Gamez-Corrales R, Séréro Y, Molino F, Lindner P (2001) Shear-induced micellar growth in dilute surfactant solutions. *EPL (Europhys Lett)* 54(5):605–611. <https://doi.org/10.1209/epl/i2001-00335-x>
- Burger C, Hsiao BS, Chu B (2010) Preferred orientation in polymer fiber scattering. *Polym Rev* 50(1):91–111. <https://doi.org/10.1080/15583720903503494>
- Calabrese MA, Rogers SA, Murphy RP, Wagner NJ (2015) The rheology and microstructure of branched micelles under shear. *J Rheol* 59(5):1299–1328. <https://doi.org/10.1122/1.4929486>
- Castelletto V, Hamley IW (2006) Capillary flow behavior of worm-like micelles studied by small-angle X-ray scattering and small angle light scattering. *Polym Adv Technol* 17(3):137–144. <https://doi.org/10.1002/pat.712>
- Castelletto V, Parras P, Hamley IW, Bäverböck P, Pedersen JS, Panine P (2007) Wormlike micelle formation and flow alignment of a pluronic block copolymer in aqueous solution. *Langmuir* 23(13):6896–6902. <https://doi.org/10.1021/la700382y>
- Cates ME, Candau SJ (1990) Statics and dynamics of worm-like surfactant micelles. *J Phys Condens Matter* 2(33):6869–6892. <https://doi.org/10.1088/0953-8984/2/33/001>
- Chatterjee T, Nakatani AI, Van Dyk AK (2014) Shear-dependent interactions in hydrophobically modified ethylene oxide urethane (HEUR) based rheology modifier–latex suspensions: part 1. Molecular microstructure. *Macromolecules* 47(3):1155–1174. <https://doi.org/10.1021/ma401566k>
- Eberle APR, Porcar L (2012) Flow-SANS and Rheo-SANS applied to soft matter. *Curr Opin Colloid Interface Sci* 17(1):33–43. <https://doi.org/10.1016/j.cocis.2011.12.001>
- Fardin MA, Perge C, Taberlet N, Manneville S (2014) Flow-induced structures versus flow instabilities. *Phys Rev E* 89(1):011001. <https://doi.org/10.1103/PhysRevE.89.011001>
- Fardin M-A, Casanellas L, Saint-Michel B, Manneville S, Lerouge S (2016) Shear-banding in wormlike micelles: beware of elastic instabilities. *J Rheol* 60(5):917–926. <https://doi.org/10.1122/1.4960333>
- Fernandez-Ballester L, Thurman DW, Kornfield JA (2009) Real-time depth sectioning: isolating the effect of stress on structure development in pressure-driven flow. *J Rheol* 53(5):1229–1254. <https://doi.org/10.1122/1.3164970>
- Gaudino D, Pasquino R, Grizzuti N (2015) Adding salt to a surfactant solution: linear rheological response of the resulting morphologies. *J Rheol* 59(6):1363–1375. <https://doi.org/10.1122/1.4931114>
- Gaudino D, Pasquino R, Krieges H, Szekely N, Pyckhout-Hintzen W, Lettinga MP, Grizzuti N (2017) Effect of the salt-induced micellar microstructure on the nonlinear shear flow behavior of ionic cetylpyridinium chloride surfactant solutions. *Phys Rev E* 95(3):032603. <https://doi.org/10.1103/PhysRevE.95.032603>
- Granek R, Cates ME (1992) Stress relaxation in living polymers: results from a Poisson renewal model. *J Chem Phys* 96(6):4758–4767. <https://doi.org/10.1063/1.462787>
- Haward SJ, Galindo-Rosales FJ, Ballesta P, Alves MA (2014) Spatiotemporal flow instabilities of wormlike micellar solutions in rectangular microchannels. *Appl Phys Lett* 104(12):124101. <https://doi.org/10.1063/1.4869476>
- Higgins JS, Benoit HC, Benoit H (1994) *Polymers and neutron scattering*. Clarendon Press, Oxford
- Hudson SD, Sarangapani P, Pathak JA, Migler KB (2015) A microliter capillary rheometer for characterization of protein solutions. *J Pharm Sci* 104(2):678–685. <https://doi.org/10.1002/jps.24201>
- Kline S (2006) Reduction and analysis of SANS and USANS data using IGOR Pro. *J Appl Crystallogr* 39(6):895–900. <https://doi.org/10.1107/S0021889806035059>
- Koehler RD, Raghavan SR, Kaler EW (2000) Microstructure and dynamics of wormlike micellar solutions formed by mixing cationic and anionic surfactants. *J Phys Chem B* 104(47):11035–11044. <https://doi.org/10.1021/jp0018899>
- Krishnamurthy VV, Bhandar AS, Piao M, Zoto I, Lane AM, Nikles DE et al (2003) Shear- and magnetic-field-induced ordering in magnetic nanoparticle dispersion from small-angle neutron scattering. *Phys Rev E* 67(5):051406. <https://doi.org/10.1103/PhysRevE.67.051406>
- Liberatore MW, Nettesheim F, Wagner NJ, Porcar L (2006) Spatially resolved small-angle neutron scattering in the 1–2 plane: a study of shear-induced phase-separating wormlike micelles. *Phys Rev E* 73(2):020504. <https://doi.org/10.1103/PhysRevE.73.020504>
- Lindner P, Bewersdorff HW, Heen R, Sittart P, Thiel H, Langowski J, Oberthür R (1990) Drag-reducing surfactant solutions in laminar and turbulent flow investigated by small-angle neutron scattering and light scattering. In: Zulauf M, Lindner P, Terech P (eds) *Trends in colloid and interface science IV*. Steinkopff, Darmstadt, pp 107–112. <https://doi.org/10.1007/BFb0115534>
- Lopez CG, Watanabe T, Martel A, Porcar L, Cabral JT (2015) Microfluidic-SANS: flow processing of complex fluids. *Sci Rep* 5:7727. <https://doi.org/10.1038/srep07727> <https://www.nature.com/articles/srep07727#supplementary-information>
- Lutz-Bueno V, Kohlbrecher J, Fischer P (2013) Shear thickening, temporal shear oscillations, and degradation of dilute equimolar CTAB/NaSal wormlike solutions. *Rheol Acta* 52(4):297–312. <https://doi.org/10.1007/s00397-012-0672-4>
- Magid LJ, Li Z, Butler PD (2000) Flexibility of elongated sodium dodecyl sulfate micelles in aqueous sodium chloride: a small-angle neutron scattering study. *Langmuir* 16(26):10028–10036. <https://doi.org/10.1021/la0006216>
- Maranzano BJ, Wagner NJ (2002) Flow-small angle neutron scattering measurements of colloidal dispersion microstructure evolution through the shear thickening transition. *J Chem Phys* 117(22):10291–10302. <https://doi.org/10.1063/1.1519253>
- Mason TG, Wilking JN, Meleson K, Chang CB, Graves SM (2006) Nanoemulsions: formation, structure, and physical properties. *J Phys Condens Matter* 18(41):R635–R666. <https://doi.org/10.1088/0953-8984/18/41/R01>
- Méndez-Sánchez AF, López-González MR, Rolón-Garrido VH, Pérez-González J, de Vargas L (2003) Instabilities of micellar systems under homogeneous and non-homogeneous flow conditions. *Rheol Acta* 42(1):56–63. <https://doi.org/10.1007/s00397-002-0254-y>
- Moon D, Migler KB (2009) Measurement of dynamic capillary pressure and viscosity via the multi-sample micro-slit rheometer. *Chem Eng Sci* 64(22):4537–4542. <https://doi.org/10.1016/j.ces.2009.02.039>
- Morozov AN, van Saarloos W (2007) An introductory essay on subcritical instabilities and the transition to turbulence in visco-elastic parallel shear flows. *Phys Rep* 447(3–6):112–143. <https://doi.org/10.1016/j.physrep.2007.03.004>

- Noirez L, Lapp A (1997) Shear flow induced transition from liquid-crystalline to polymer behavior in side-chain liquid crystal polymers. *Phys Rev Lett* 78(1):70–73. <https://doi.org/10.1103/PhysRevLett.78.70>
- Pakdel P, McKinley GH (1996) Elastic instability and curved streamlines. *Phys Rev Lett* 77(12):2459–2462. <https://doi.org/10.1103/PhysRevLett.77.2459>
- Pedersen JS (1997) Analysis of small-angle scattering data from colloids and polymer solutions: modeling and least-squares fitting. *Adv Colloid Interf Sci* 70:171–210. [https://doi.org/10.1016/S0001-8686\(97\)00312-6](https://doi.org/10.1016/S0001-8686(97)00312-6)
- Pedersen JS, Schurtenberger P (1996) Scattering functions of semiflexible polymers with and without excluded volume effects. *Macromolecules* 29(23):7602–7612. <https://doi.org/10.1021/ma9607630>
- Penfold J, Staples E, Tucker I, Carroll P, Clayton I, Cowan JS et al (2006) Elongational flow induced ordering in surfactant micelles and mesophases. *J Phys Chem B* 110(2):1073–1082. <https://doi.org/10.1021/jp051122m>
- Pipe CJ, McKinley GH (2009) Microfluidic rheometry. *Mech Res Commun* 36(1):110–120. <https://doi.org/10.1016/j.mechrescom.2008.08.009>
- Pipe CJ, Majmudar TS, McKinley GH (2008) High shear rate viscometry. *Rheol Acta* 47(5):621–642. <https://doi.org/10.1007/s00397-008-0268-1>
- Porte G, Gomati R, El Haitamy O, Appell J, Marignan J (1986) Morphological transformations of the primary surfactant structures in brine-rich mixtures of ternary systems (surfactant/alcohol/brine). *J Phys Chem* 90(22):5746–5751. <https://doi.org/10.1021/j100280a055>
- Rehage H, Hoffmann H (1991) Viscoelastic surfactant solutions: model systems for rheological research. *Mol Phys* 74(5):933–973. <https://doi.org/10.1080/00268979100102721>
- Salipante PF, Little CAE, Hudson SD (2017) Jetting of a shear banding fluid in rectangular ducts. *Phys Rev Fluids* 2(3):033302. <https://doi.org/10.1103/PhysRevFluids.2.033302>
- Singh I, Themistou E, Porcar L, Neelamegham S (2009) Fluid shear induces conformation change in human blood protein von Willebrand factor in solution. *Biophys J* 96(6):2313–2320. <https://doi.org/10.1016/j.bpj.2008.12.3900>
- Squires TM, Quake SR (2005) Microfluidics: fluid physics at the nanoliter scale. *Rev Mod Phys* 77(3):977–1026. <https://doi.org/10.1103/RevModPhys.77.977>
- Takeda M, Kusano T, Matsunaga T, Endo H, Shibayama M, Shikata T (2011) Rheo-SANS studies on shear-thickening/thinning in aqueous rodlike micellar solutions. *Langmuir* 27(5):1731–1738. <https://doi.org/10.1021/la104647u>
- Tang M-Y, Fellers JF, Lin JS (1984) New treatment of the theory for small-angle x-ray scattering with applications to polystyrene crazes. *J Polym Sci Polym Phys Ed* 22(12):2215–2241. <https://doi.org/10.1002/pol.1984.180221219>
- Vogt K, Beaucage G, Weaver M, Jiang H (2015) Scattering function for branched wormlike chains. *Langmuir* 31(30):8228–8234. <https://doi.org/10.1021/acs.langmuir.5b01630>
- Walker LM (2001) Rheology and structure of worm-like micelles. *Curr Opin Colloid Interface Sci* 6(5–6):451–456. [https://doi.org/10.1016/S1359-0294\(01\)00116-9](https://doi.org/10.1016/S1359-0294(01)00116-9)
- Weigandt KM, Porcar L, Pozzo DC (2011) In situ neutron scattering study of structural transitions in fibrin networks under shear deformation. *Soft Matter* 7(21):9992–10000. <https://doi.org/10.1039/C1SM06176C>
- Wilking JN, Chang CB, Fryd MM, Porcar L, Mason TG (2011) Shear-induced disruption of dense nanoemulsion gels. *Langmuir* 27(9):5204–5210. <https://doi.org/10.1021/la200021r>
- Zou W, Larson RG (2014) A mesoscopic simulation method for predicting the rheology of semi-dilute wormlike micellar solutions. *J Rheol* 58(3):681–721. <https://doi.org/10.1122/1.4868875>
- Zou W, Tang X, Weaver M, Koenig P, Larson RG (2015) Determination of characteristic lengths and times for wormlike micelle solutions from rheology using a mesoscopic simulation method. *J Rheol* 59(4):903–934. <https://doi.org/10.1122/1.4919403>